Highlights

Inverse design of cavities for Bloch Surface Waves interfaced to integrated waveguides

Yannick Augenstein, Matthieu Roussey, Thierry Grosjean, Emiliano Descrovi, Carsten Rockstuhl

- Efficient coupling of cavity emissions and waveguides in Bloch Surface Wave platforms
- Effective index simulations make topology optimization feasible for large systems

Inverse design of cavities for Bloch Surface Waves interfaced to integrated waveguides

Yannick Augenstein[a,], Matthieu Roussey[e], Thierry Grosjean[d], Emiliano Descrovi[c], Carsten Rockstuhl[a,b]

[a]*Karlsruhe Institute of Technology, Institute of Theoretical Solid State Physics, Wolfgang-Gaede-Str. 1, Karlsruhe, 76131, Germany*
[b]*Karlsruhe Institute of Technology, Institute of Nanotechnology, Hermann-von-Helmholtz-Platz 1, Eggenstein-Leopoldshafen, 76344, Germany*
[c]*Politecnico di Torino, Department of Applied Science and Technology, Corso Duca degli Abruzzi 24, Torino, 10129, Italy*
[d]*FEMTO-ST Institute, Department of Optics, UMR CNRS 6174, 15B Avenue des Montboucons, Besançon, 25030, France*
[e]*Institute of Photonics, Department of Physics and Mathematics, University of Eastern Finland, PO Box 111, Joensuu, 80101, Finland*

Abstract

The design of functional elements for Bloch Surface Waves (BSW) is challenging because of the relatively low index contrast offered by the respective platforms. Here, we design a supporting photonic nanostructure that extracts as much light as possible from a quantum emitter into a waveguide in an integrated BSW architecture. The inverse problem is solved using topology optimization. Emphasis is put on discussing the algorithm's emerging strategies for the design to enhance the Purcell factor, the coupling efficiency, or both for different index contrasts. Fully three-dimensional simulations of an explicit device show the benefits of our devices and pave the way for integrating such unconventional photonic elements into future fully-integrated BSW devices.

Keywords: effective index, surface waves, inverse design, Purcell effect

---

[*] Corresponding author
Email address: `yannick.augenstein@kit.edu` (Yannick Augenstein)

Preprint submitted to PNFA *November 15, 2022*

1. Introduction

Bloch Surface Waves (BSW) are evanescent eigensolutions to Maxwell's equations, propagating parallel to the interface between an isotropic medium and a truncated one-dimensional photonic crystal (1DPC) [1, 2]. Interestingly, they exhibit the highest amplitude close to the 1DPC surface and they can be either TE or TM polarized [3]. The one-dimensional photonic crystal is typically implemented as a layer stack of dielectric materials with an alternating refractive index. In particular, BSWs are operated in the frequency domain of the band gap of the one-dimensional photonic crystal. This guarantees an exponentially decaying field in the homogeneous medium (e.g. air, water, etc.) and an oscillating amplitude with an exponentially decaying envelope in the layered medium, resulting in long propagation lengths. Although the underlying physics is rather different, BSWs bear many similarities to other guided surface modes, such as propagating surface plasmon polaritons [4, 5], in that they are localized to the interface. The field localization is less pronounced since the effective index of the guided modes will not exceed those of the indices of the involved materials and tends to be relatively small in practical situations. However, BSWs offer in exchange the fantastic opportunity to reach propagation lengths in the order of many hundreds of micrometers or even millimeters, while still having the field largely extending in the outer medium [6, 7]. This is possible because dissipation losses in the all-dielectric platform do not limit their propagation lengths. Instead, the propagation length is frequently only limited by the finite number of layers used to build the photonic crystal [8]. In fact, a limited number of layers causes some leakage radiation due to evanescent tunneling toward the substrate beneath the multilayer, but it can be considered as an engineering problem to suppress it.

The ability to guide light over macroscopic distances in an integrated architecture enables a plethora of applications that serve societal needs [9, 10]. Examples of functional devices explored in the past range from on-chip information processing components [11] to sensing platforms [12, 13, 14]. Such sensors can even be deposited on the end-facets of fibers to be extremely flexible [15, 16]. A crucial component to exploit BSWs in integrated circuits is their confinement into a second dimension, i.e., the one tangential to the substrate interface and normal to the propagation direction [17]. This is usually achieved by patterning the terminating layer of the one-dimensional photonic crystal, frequently called the functional layer, such that for the operational frequency, the BSWs experience slightly different effective indices in the structured and unstructured functional layer, respectively [18]. This permits to achieve waveguides and resonators with lateral confinement [19, 20], but also more complicated functional devices that can be realized upon exploitation of the generally small index contrast [21].

Nevertheless, the tiny index difference, which is frequently only in the order of $\Delta n \approx 0.1$, constitutes a prime design challenge [22, 23]. It implies that the direct application of conventional optical components, e.g., even just a lens, is not straightforward, as the design of these components usually hinges on a larger index contrast. Consequently, and entirely in the spirit of the current special issue to which this article aims to contribute, the design of functional components for an integrated BSW architecture is a wonderful playground to explore the application of novel computational approaches for inverse design [24]. Only with such strategies, it is possible to identify feasible designs that serve a well-defined purpose while fully respecting the constraints imposed by the limited index contrast. While a large variety of different methodologies exist to solve the inverse problem [25, 26, 27, 28, 29, 30, 31, 32, 33, 34, 35, 36, 37, 38, 39, 40, 41, 42], we exploit topology optimization here.

We apply topology optimization to contribute to an essential step for the further development of a BSW-based integrated photonic architecture. Our exploration concerns the extraction of light emitted from an embedded source into a BSW-integrated circuit. The circuit consists of, for simplicity, the form of a waveguide. The embedded source, considered as an electric dipolar emitter, is assumed to be externally pumped and shall release as much energy as possible into the waveguide. The structure at stake in our consideration is a finite domain surrounding the emitter that can be structured and shall direct as much light as possible into the waveguide. Two aspects must be kept in mind that deny simple solutions and prompt the application of advanced tools to solve the inverse design problem. First, the coupling efficiency needs to be maximized. The coupling efficiency is the fraction of the emitted light that finds its way into the waveguide. Second, the supporting structure can contribute to a Purcell enhancement, i.e. the dipole-waveguide coupler must be resonant. The Purcell enhancement measures the increased local density of states to extract the radiation from the emitters. It is defined as the power extracted from the source in the presence of the supporting photonic structure normalized to the power extracted from the source in free space (or some other referential structure). The higher the Purcell enhancement [43] and the quicker the light is extracted, the faster the emitter can be excited again to release a further photon. The scientific challenge that we wish to explore concerns the discussion of how a suitable supporting photonic structure should look to transfer as much light from a quantum emitter into a waveguide through coupling to the supported BSWs assuming a dipole excitation in saturation regime. Emphasis is put on studying that effect depending on the index contrast the BSW platform offers to shed light on the interplay between the two effects that dominate the response. Topology optimization is used for the inverse design of the supporting photonic structure.

The article is structured into three sections. In Section 2, we discuss the setting of our inverse design problem and detail the used computational techniques. In Section 3, we present the results and discussion. We systematically study the details of the optimized devices initially in a 2D setting but verify the optimizations in full 3D simulations. The discussion orients on the question of how the details of the optimized structure vary by changing the possible index contrast. In Section 4, we conclude on our results.

2. Optimization setup

We aim to optimize functional photonic devices that can extract light emitted by a dipole-like source that couples into a surface mode sustained by a dielectric multi-layer stack into a waveguide (see Fig. 1) such that it can be used for, e.g., on-chip light sources. However, the system under consideration is relatively large, rendering an optimization using full-wave 3D simulations impractical. Instead, we transform the problem into a 2D one by using an effective index method, which has been applied successfully in the past to the simulation and design of functional devices for manipulating BSWs [44, 45, 46] due to the low refractive index contrast of such systems.

In the proposed setup, the dipole source is oriented along the x direction and emits light with a Gaussian spectrum centered at a wavelength of $\lambda_0 = 570\,\mathrm{nm}$ placed at the center of the spacer region (black circle). We define a circular design region as shown in Fig. 1 with a radius of $5.7\,\mu\mathrm{m}$ and define our objective function F as

$$F = |\alpha_0|^2 \quad , \tag{1}$$

where α_0 is the mode coefficient of the fundamental forward-propagating TM-polarized mode (in-plane electric field) of the waveguide, normalized such that $|\alpha_0|^2$ corresponds to the power carried in that mode.

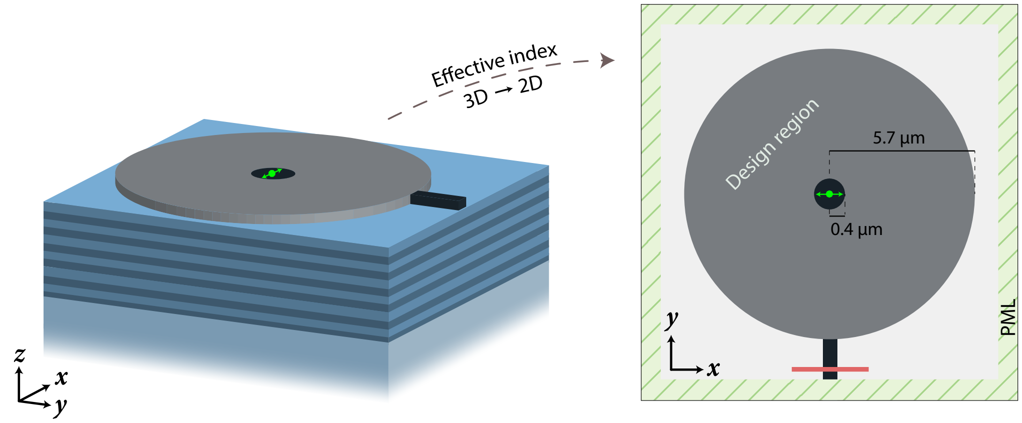

Figure 1: Full sketch of a prototypical material platform that supports BSWs (left). A functional layer is patterned on top of a dielectric multi-layer structure sitting on a substrate in this conceptual setting. The optimization setup for the 2D effective index simulation (right) consists of a circular design region with a radius of 5.7 µm and a central spacer region with a radius of 0.4 µm and fixed material distribution. The x-polarized dipole source is embedded in the center of the spacer region. A waveguide with a width of 0.3 µm extends out from the lower edge of the design region. The optimization aims to maximize the power coupled from the dipole into the fundamental TM-polarized mode of the connected waveguide.

We use a standard filter-and-project parametrization [47, 48, 49] and use the method of moving asymptotes (MMA) [50] as implemented in nlopt [51] (version 2.7.1) for constrained, nonlinear topology optimization. The designs are discretized on a 2D grid with a resolution of 100 $\frac{\text{px}}{\mu\text{m}}$. To parametrize the designs, the dimensionless design variables $\rho \in [0, 1]$ are first low-pass filtered using a Gaussian kernel to impose a minimum feature size of 50 nm. Afterward, a soft-thresholding function is applied to promote binary solutions in the optimization:

$$\hat{\rho} = \frac{\tanh(\beta/2) + \tanh(\beta\,(\rho - 0.5))}{2\,\tanh(\beta/2)} \quad . \tag{2}$$

The parameter β dictates the strength of the binarization and is increased in multiple steps during the optimization process to yield final, binary designs. To prevent the optimization from reverting to less binary designs, we constrain the gray indicator

$$c_{\mathrm{g}}(\hat{\boldsymbol{\rho}}) = \frac{1}{n} \sum_{i=1}^{n} 4\hat{\rho}_i\,(1 - \hat{\rho}_i) \tag{3}$$

suggested in [52] to be smaller than a threshold γ, which is determined from the design directly after increasing β. After projection, a circular mask is applied to the design variables such that the device is constrained to a circular geometry. The device geometries are then linearly interpolated to their respective refractive indices, and the simulations are performed using Meep [53]. The sensitivities of the objective function w.r.t. the parametrization are obtained using Meep's adjoint module [54], and the sensitivities of the parametrization w.r.t. the optimization variables ρ are obtained using autograd [55].

We then formulate the optimization problem as:

$$\max_{\boldsymbol{\rho}} \quad |\alpha_0|^2 \tag{4a}$$

$$\text{s.t.} \quad \alpha_0 = \int_S \left[\tilde{\mathbf{E}}^*(\boldsymbol{r}) \times \tilde{\mathbf{H}}_0(\boldsymbol{r}) + \tilde{\mathbf{E}}_0(\boldsymbol{r}) \times \tilde{\mathbf{H}}^*(\boldsymbol{r})\right] \cdot \hat{\mathbf{n}} \,\mathrm{d}A \tag{4b}$$

$$c_\mathrm{g}(\hat{\boldsymbol{\rho}}) - \gamma \leq 0 \tag{4c}$$

$$0 \leq \boldsymbol{\rho} \leq 1 \quad , \tag{4d}$$

where $\tilde{\mathbf{E}}$, $\tilde{\mathbf{H}}$ in Eq. 4b are the Fourier-transformed fields at the target wavelength of 570 nm at the mode monitor (c.f. Fig. 1) and $\tilde{\mathbf{E}}_0$, $\tilde{\mathbf{H}}_0$ are the fields corresponding to the fundamental mode in the waveguide (obtained using the eigenmode solver MPB [56]).

The effective index of the surface mode without the functional layer is assumed to be $n_{\mathrm{eff},0} = 1.019$, and we perform the optimization for different effective index contrasts Δn_eff ranging from 0.01 to 0.13 in increments of 0.01. For the device with the highest index contrast $\Delta n_\mathrm{eff} = 0.13$, the surface mode with the functional layer has an effective index of $n_{\mathrm{eff},1} = 1.149$, which corresponds to the material platform presented in [46].

The 2D simulations in the optimization are performed using MPI-parallel Meep (version 1.23.0) on a desktop computer with a 10-core CPU (Intel Core i9-10900 @ 2.80 GHz) at a resolution of $50\,\frac{\mathrm{px}}{\mathrm{\mu m}}$.

3. Results and discussion

3.1. Optimization and evaluation in 2D

By running multiple optimizations for different effective refractive index contrasts in the range of $\Delta n_\mathrm{eff} = 0.01$ to 0.13, we can numerically study

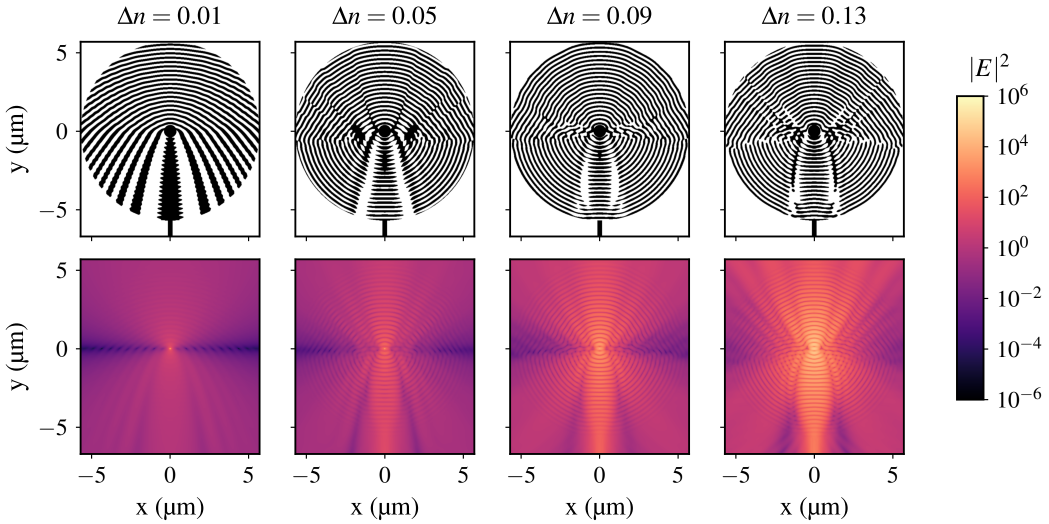

Figure 2: Optimized device designs (top row) and corresponding electric field intensities (bottom row) in log scale at the target wavelength of 570 nm. Shown here are four selected devices designed for different effective index contrasts (columns). Note that a short length of waveguide is included for clarity but it is not part of the design region.

the implications on achievable device performance resulting from different conceivable surface-wave sustaining material platforms.

The results of the optimization for four selected devices and the corresponding electric field intensities (log scale) are shown in Fig. 2.

For all designs, we observe that the optimization forms a kind of distributed Bragg reflector (DBR), most notably in the upper half-space of the design. Such a solution to the optimization problem is reasonably intuitive, as the absolute power coupled into the waveguide, regardless of any additional coupling elements, is directly proportional to the power emitted by the source. It is thus a natural and expected solution that the optimization would converge towards designs that, at least in part, form an electromagnetic cavity. The coupling of the power emitted by the source to the waveguide is, of course, not only governed by the total power emitted but also by the efficiency with which the device can guide the field towards the waveguide. This efficiency, in turn, is limited by the refractive index contrast available for steering the electromagnetic fields. As the refractive index contrast becomes larger, the device can more efficiently make use of finer spatial variations in the patterned layer to guide the light, an observation that is evident when examining the different devices in Fig. 2.

The device for $\Delta n = 0.01$ features a mostly adiabatic transition from the DBR in the upper half-space of the design to a tapered waveguide-like element. That is a clear indication that light emitted in the upper half-space should be back-reflected, but otherwise it is primarily of importance to increase the coupling efficiency towards the waveguide by steering the light into the right direction. A possible enhancement of the emission due to some cavity effect is not really visible. But that is also not surprising considering the very low index contrast that leads to cavities with small quality factors.

The device for $\Delta n = 0.13$ exhibits a more intricate and non-intuitive design. The central part of its design consists of multiple sub-wavelength elements, and the waveguide-like structure in the lower half-space has made way for a more intricate design. In the essence the upper part continues to leave the impression as acting like a DBR but the lower part, i.e. the part between the source the waveguide, clearly balances our requirements now in terms of a good coupling efficiency and a high enhancement of the extracted power.

To quantify the performance of the optimized devices, we investigate the Purcell enhancement of the source in the spacer region and the coupling efficiency into the waveguide. We obtain spectra in the range (570 ± 30) nm for all optimized devices in Fig. 3 and we show the obtained values at the target wavelength of 570 nm separately in Fig. 4. The Purcell enhancement

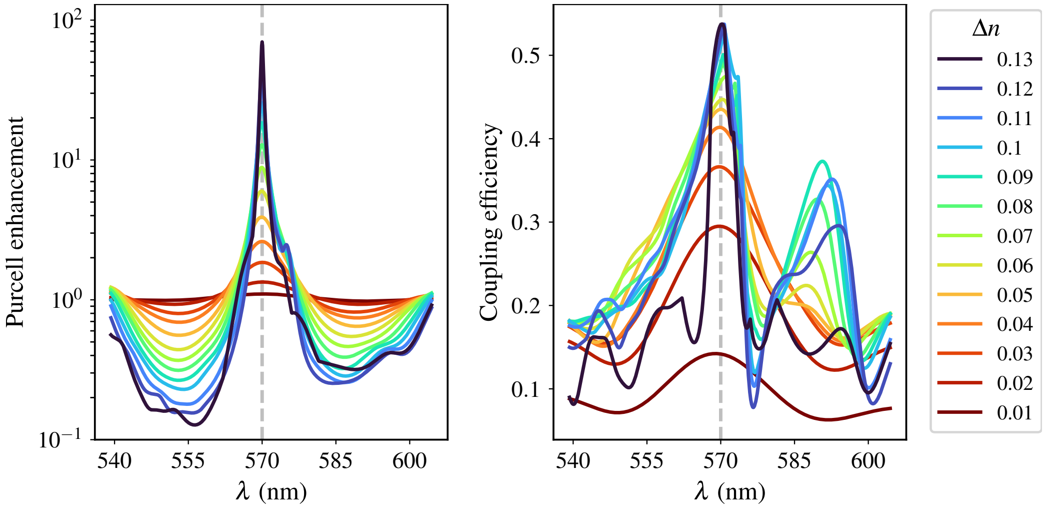

Figure 3: Spectra of Purcell enhancement (left) and coupling efficiencies (right) for all designs as obtained from the 2D effective index setup in which the devices were optimized.

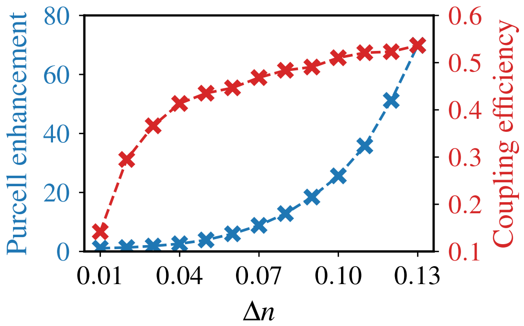

Figure 4: Purcell enhancement and coupling efficiency for all designs at the target wavelength of 570 nm obtained from 2D effective index simulations.

is calculated as the ratio of power flow from the source in the device ("cavity") and a homogeneous medium ($n_{\mathrm{eff},1}$). The power flow is obtained by placing a box of flux monitors with an edge length of 0.5 µm around the source and accumulating the appropriate Fourier-transformed fields. Similarly, the coupling efficiency is obtained as the ratio of the power contained in the fundamental mode of the waveguide with

$$P_{\mathrm{mode}} = |\alpha_0|^2 \tag{5}$$

and the power emitted by the source.

The optimized devices clearly show a Purcell enhancement at the target wavelength, with the $\Delta n = 0.01$ device having a Purcell factor of approximately 2, increasing exponentially with increasing Δn (c.f. Fig. 4) up to the $\Delta n = 0.13$ device with a Purcell enhancement of around 70. We also see that the designs with higher index contrast exhibit better coupling efficiency, with the $\Delta n = 0.13$ design achieving the highest coupling efficiency at 54 %. Notably, the higher index contrast designs exhibit much more significant wavelength specificity than the lower index designs, which show a more broadband response. This reinforces the previous consideration that due to the higher index contrast, the optimization can more specifically tailor the "guiding performance" of the device to the target wavelength, which at very low index contrasts yields only diminishing returns. Further, we observe that the coupling efficiency increases substantially between $\Delta n = 0.01$ and $\Delta n = 0.04$ and then slowly saturates at higher contrasts at values around 0.5. This is likely owed to the fact that, while there is a significant gap in performance between the devices optimized for extremely low index contrasts ($\Delta n \approx 0.01$) and those at moderate contrasts ($\Delta n \approx 0.1$), the index contrast of all optimized devices is still relatively low. Thus, a significant portion of the radiation emitted by the dipole is lost in the upper half-space of the design. These insights mirror the discussion that was phenomenologically made when looking into the different designs obtained for a different index contrast.

3.2. Comparison between 2D and 3D

So far, we have examined the performance of the optimized devices in 2D, i.e., in the setting of the effective index approximation of the surface mode that they were optimized for. However, it is crucial to test whether this approximation holds for the optimized devices in the 3D setting that was envisioned. To do this, we adopt the dielectric multi-layer stack from [46]. The material platform consists of a sequence of Silica and Tantalia slabs deposited on a glass substrate ($n_{\text{glass}} = 1.5$), with a final layer of PMMA into which the device geometry is patterned. The layer stack consists of ten alternating layers of Ta_2O_5 ($n_{Ta_2O_5} = 2.08$, $d_{Ta_2O_5} = 95\,\text{nm}$) and SiO_2 ($n_{SiO_2} = 1.46$, $d_{SiO_2} = 137\,\text{nm}$), an additional layer of Ta_2O_5, and a layer of SiO_2 with a thickness of 127 nm. The final PMMA layer has a refractive index of $n_{\text{PMMA}} = 1.48$ with a thickness of 75 nm. All materials are assumed to be free of dispersion across the wavelength range in question ($(570 \pm 30)\,\text{nm}$). The effective index of the surface mode at 570 nm supported by this system without the PMMA layer is $n_{\text{eff},0} = 1.019$ and $n_{\text{eff},1} = 1.149$ with the PMMA layer. This corresponds to the effective indices for which the $\Delta n = 0.13$ device was designed. We extrude the optimized 2D design 75 nm in the z-direction to use it as the functional PMMA layer. The x-polarized dipole source is embedded at the center of the spacer region inside of the PMMA layer 35 nm beneath the surface. The 3D simulation is then run using FDTD (Meep) at a resolution of $80\,\mu\text{m}^{-1}$ parallelized over 76 CPU cores (2x Intel Xeon Platinum 8368 @ 2.4 GHz), taking 16.5 hours. Analogous to the 2D simulations previously, the power flow from the dipole is monitored in all spatial directions using flux monitor planes with an edge length of $0.5\,\mu\text{m}$ for both the homogeneous bulk PMMA as well as the patterned medium and both the Purcell enhancement as well as the coupling efficiency are calculated as before.

The comparison between the full-wave 3D simulation and that of the corresponding 2D effective index simulation is shown in Fig. 5. While there are apparent differences between both approaches, we see a marked increase in the Purcell enhancement and the coupling efficiency at the target wavelength

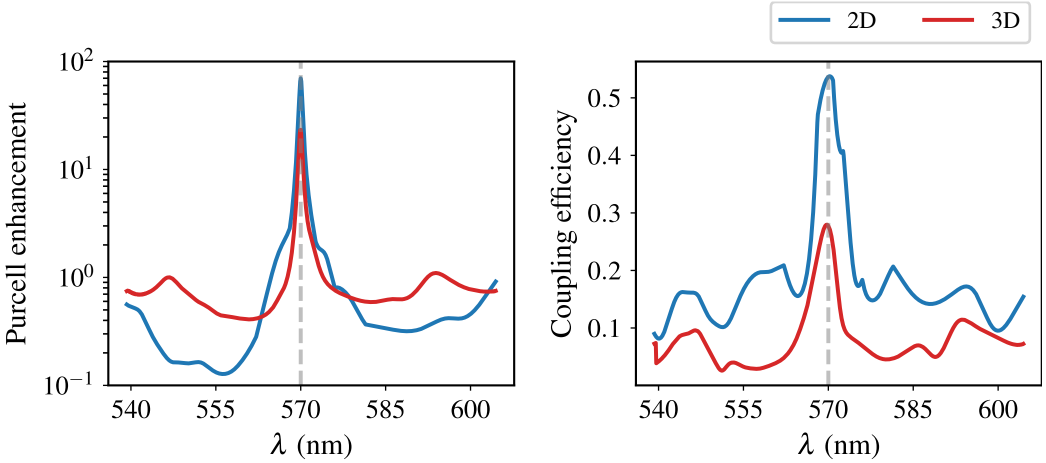

Figure 5: Comparison of the Purcell enhancement (left) and the coupling efficiency (right) between the 2D effective index simulation and a 3D full-wave simulation. The device was optimized for an effective index contrast of $\Delta n = 0.13$, which corresponds to the material platform presented in [46].

of the optimization in the 3D results. While the Purcell factor in 2D was calculated to be 70, the Purcell enhancement in 3D is reduced to a factor of 23. This is not surprising, as the effective index simulations entirely neglect out-of-plane scattering losses. A large part of the radiation emitted by the source is emitted out-of-plane, which is neither captured by the patterned PMMA layer in 3D nor accounted for in the 2D simulations. However, the analytically constructed DBR structure from [46] achieves a Purcell factor of 32. As our optimized device represents a compromise between the Purcell enhancement and the coupling efficiency, it is expected that such a device will exhibit a lower enhancement since energy is continually extracted from the system. This indicates that while there is a mismatch in terms of absolute numbers between the 2D and 3D simulations, the devices optimized using the effective index method achieve reasonably good performance in 3D. A similar argument can be made for the observed coupling efficiency, which is 0.54 in 2D and 0.28 in 3D, in that a significant portion of the light emitted from the dipole is lost to out-of-plane scattering, i.e not coupled to BSW, which in turn limits the amount of power that can be coupled into the BSW waveguide. However, since the structure is only patterned in the PMMA layer, the degrees of freedom even in the 3D setup are effectively two-dimensional as there is no patterning in the z-direction. As such, the additional losses incurred in the 3D case can be assumed to be of similar magnitude between different devices when switching between the 2D effective index setup and the full 3D geometry, indicating that the optimized structures are still close to optimal even in the 3D case.

There is also the aspect of practicality – a single 3D simulation at sufficiently high resolution takes around 16 hours to complete on a high-performance computer. To calculate the sensitivities via the adjoint method, an additional simulation is needed at every iteration, increasing the time for a single gradient-based update step to around 32 hours if done with a 3D full-wave simulation. A typical optimization of the presented devices needs a few hundred such iterations, rendering a full optimization entirely infeasible. On the other hand, the effective index simulations take roughly 30 seconds per simulation on a mid-range desktop computer while yielding designs that still exhibit good performance. A possible compromise could be the optimization of devices using the effective index method and refining the converged solution for a few steps using a full-wave simulation. However, even just ten of such refinement steps would take on the order of weeks in the demonstrated setup and would be beyond the scope of this work.

There exists also the possibility of tackling the stated design problem with different approaches, as there has been much exciting work on the inverse design of photonic devices, both in 2D and 3D, in recent years. However, we note that the computational cost in our optimization stems almost exclusively from the cost of performing the simulations. While many alternative optimization schemes exist, none of them (to our knowledge) remove the cost of numerical simulations.

Gradient-free methods such as swarm or evolutionary optimization rely on extensive sampling of the solution space, which means doing many numerical simulations [28, 57, 34, 38]. These methods can perform very well when gradients are not unavailable (e.g., for discrete optimization problems), but generally need to sample the objective function more often than gradient-based methods simply due to having less information about the objective function.

Data-driven approaches, such as machine learning, tend to “front-load” the computational cost of performing the simulations into the generation of a dataset with which, e.g., a fast surrogate solver is trained [58, 59, 60]. This can be useful when one needs to perform similar tasks many times, or when the dataset can be repurposed for a variety of tasks, but the trade-off is that the number of samples required for generating a sufficiently large dataset usually exceeds the number of simulations one would need to perform to solve only one, or a few, of these tasks.

Thus, we argue that all such methods are fundamentally bound by the speed with at which one can perform the relevant simulations. In our work, we propose using effective index simulations in 2D instead of full-wave 3D simulations as a means to speed up the optimization process by orders of magnitude, at the cost of sacrificing some accuracy in the simulation results.

4. Conclusions

We have demonstrated the use of topology optimization for the inverse design of devices that efficiently extract light from a dipole source into a waveguide in a low index contrast setting, as is typical for dielectric systems with surface modes. In our approach, we approximate the 3D system with an effective index method and numerically compare the performance of one of the optimized devices with its expected performance in an established experimental platform, showing a significant increase in both the Purcell enhancement and the coupling efficiency in the 3D case. The proposed devices open the door to the integration of spontaneous light emission with integrated photonic circuits and present a new way of manipulating the propagation of BSWs.

Acknowledgments

Y.A. and C.R. acknowledge support from the German Research Foundation within the Excellence Cluster 3D Matter Made to Order (EXC 2082/1 under project number 390761711) and by the Carl Zeiss Foundation. M.R. acknowledges the Academy of Finland Flagship PREIN, decision 320166. Part of this work was performed on the HoreKa supercomputer funded by the Ministry of Science, Research and the Arts Baden-Württemberg and the Federal Ministry of Education and Research.

References

[1] R. D. Meade, K. D. Brommer, A. M. Rappe, J. Joannopoulos, Electromagnetic bloch waves at the surface of a photonic crystal, Physical Review B 44 (19) (1991) 10961.

[2] P. Yeh, A. Yariv, C.-S. Hong, Electromagnetic propagation in periodic stratified media. i. general theory, JOSA 67 (4) (1977) 423–438.

[3] J. Chen, D. Zhang, P. Wang, H. Ming, J. R. Lakowicz, Strong polarization transformation of bloch surface waves, Phys. Rev. Applied 9 (2018) 024008.

[4] A. V. Zayats, I. I. Smolyaninov, A. A. Maradudin, Nano-optics of surface plasmon polaritons, Physics reports 408 (3-4) (2005) 131–314.

[5] W. L. Barnes, Surface plasmon–polariton length scales: a route to subwavelength optics, Journal of optics A: pure and applied optics 8 (4) (2006) S87.

[6] R. Wang, Y. Wang, D. Zhang, G. Si, L. Zhu, L. Du, S. Kou, R. Badugu, M. Rosenfeld, J. Lin, et al., Diffraction-free bloch surface waves, ACS nano 11 (6) (2017) 5383–5390.

[7] B. Vosoughi Lahijani, N. Descharmes, R. Barbey, G. D. Osowiecki, V. J. Wittwer, O. Razskazovskaya, T. Südmeyer, H. P. Herzig, Centimeter-scale propagation of optical surface waves at visible wavelengths, Advanced Optical Materials 10 (10) (2022) 2102854.

[8] R. Dubey, E. Barakat, M. Häyrinen, M. Roussey, S. K. Honkanen, M. Kuittinen, H. P. Herzig, Experimental investigation of the propagation properties of bloch surface waves on dielectric multilayer platform, Journal of the European Optical Society-Rapid Publications 13 (1) (2017) 1–9.

[9] A. Sinibaldi, N. Danz, E. Descrovi, P. Munzert, U. Schulz, F. Sonntag, L. Dominici, F. Michelotti, Direct comparison of the performance of bloch surface wave and surface plasmon polariton sensors, Sensors and Actuators B: Chemical 174 (2012) 292–298.

[10] L. Yu, E. Barakat, T. Sfez, L. Hvozdara, J. Di Francesco, H. Peter Herzig, Manipulating bloch surface waves in 2d: a platform concept-based flat lens, Light: Science & Applications 3 (1) (2014) e124–e124.

[11] L. Doskolovich, E. Bezus, D. Bykov, V. Soifer, Spatial differentiation of bloch surface wave beams using an on-chip phase-shifted bragg grating, Journal of Optics 18 (11) (2016) 115006.

[12] P. Rivolo, F. Michelotti, F. Frascella, G. Digregorio, P. Mandracci, L. Dominici, F. Giorgis, E. Descrovi, Real time secondary antibody detection by means of silicon-based multilayers sustaining bloch surface waves, Sensors and Actuators B: Chemical 161 (1) (2012) 1046–1052.

[13] Y. Kuai, Z. Xie, J. Chen, H. Gui, L. Xu, C. Kuang, P. Wang, X. Liu, J. Liu, J. R. Lakowicz, et al., Real-time measurement of the hygroscopic growth dynamics of single aerosol nanoparticles with bloch surface wave microscopy, ACS nano 14 (7) (2020) 9136–9144.

[14] R. Wang, X. Lei, Y. Jin, X. Wen, L. Du, A. Wu, A. V. Zayats, X. Yuan, Directional imbalance of bloch surface waves for ultrasensitive displacement metrology, Nanoscale 13 (25) (2021) 11041–11050.

[15] M. Scaravilli, G. Castaldi, A. Cusano, V. Galdi, Grating-coupling-based excitation of bloch surface waves for lab-on-fiber optrodes, Optics Express 24 (24) (2016) 27771–27784.

[16] M. Scaravilli, A. Micco, G. Castaldi, G. Coppola, M. Gioffrè, M. Iodice, V. La Ferrara, V. Galdi, A. Cusano, Excitation of bloch surface waves on an optical fiber tip, Advanced Optical Materials 6 (19) (2018) 1800477.

[17] R. Wang, H. Xia, D. Zhang, J. Chen, L. Zhu, Y. Wang, E. Yang, T. Zang, X. Wen, G. Zou, et al., Bloch surface waves confined in one dimension with a single polymeric nanofibre, Nature communications 8 (1) (2017) 1–10.

[18] L. Yu, E. Barakat, W. Nakagawa, H. P. Herzig, Investigation of ultra-thin waveguide arrays on a bloch surface wave platform, JOSA B 31 (12) (2014) 2996–3000.

[19] T. Perani, D. Aurelio, M. Liscidini, Bloch-surface-wave photonic crystal nanobeam cavity, Opt. Lett. 44 (21) (2019) 5133–5136.

[20] T. Perani, M. Liscidini, Long-range bloch surface waves in photonic crystal ridges, Opt. Lett. 45 (23) (2020) 6534–6537.

[21] R. Dubey, B. V. Lahijani, M. Häyrinen, M. Roussey, M. Kuittinen, H. P. Herzig, Ultra-thin bloch-surface-wave-based reflector at telecommunication wavelength, Photonics Research 5 (5) (2017) 494–499.

[22] M.-S. Kim, B. Vosoughi Lahijani, N. Descharmes, J. Straubel, F. Negredo, C. Rockstuhl, M. Hayrinen, M. Kuittinen, M. Roussey, H. P. Herzig, Subwavelength focusing of bloch surface waves, Acs Photonics 4 (6) (2017) 1477–1483.

[23] M.-S. Kim, A. Vetter, C. Rockstuhl, B. V. Lahijani, M. Häyrinen, M. Kuittinen, M. Roussey, H. P. Herzig, Multiple self-healing bloch surface wave beams generated by a two-dimensional fraxicon, Communications Physics 1 (1) (2018) 1–8.

[24] S. Molesky, Z. Lin, A. Y. Piggott, W. Jin, J. Vucković, A. W. Rodriguez, Inverse design in nanophotonics, Nature Photonics 12 (11) (2018) 659–670.

[25] A. Y. Piggott, J. Lu, K. G. Lagoudakis, J. Petykiewicz, T. M. Babinec, J. Vučković, Inverse design and demonstration of a compact and broadband on-chip wavelength demultiplexer, Nature Photonics 9 (6) (2015) 374–377.

[26] W. Jin, S. Molesky, Z. Lin, K.-M. C. Fu, A. W. Rodriguez, Inverse design of compact multimode cavity couplers, Optics express 26 (20) (2018) 26713–26721.

[27] P.-I. Schneider, X. Garcia Santiago, V. Soltwisch, M. Hammerschmidt, S. Burger, C. Rockstuhl, Benchmarking five global optimization approaches for nano-optical shape optimization and parameter reconstruction, ACS Photonics 6 (11) (2019) 2726–2733.

[28] J. Baxter, A. Calà Lesina, J.-M. Guay, A. Weck, P. Berini, L. Ramunno, Plasmonic colours predicted by deep learning, Scientific reports 9 (1) (2019) 1–9.

[29] E. Bayati, R. Pestourie, S. Colburn, Z. Lin, S. G. Johnson, A. Majumdar, Inverse designed metalenses with extended depth of focus, ACS photonics 7 (4) (2020) 873–878.

[30] K. Wang, X. Ren, W. Chang, L. Lu, D. Liu, M. Zhang, Inverse design of digital nanophotonic devices using the adjoint method, Photonics Research 8 (4) (2020) 528–533.

[31] M. Minkov, I. A. Williamson, L. C. Andreani, D. Gerace, B. Lou, A. Y. Song, T. W. Hughes, S. Fan, Inverse design of photonic crystals through automatic differentiation, Acs Photonics 7 (7) (2020) 1729–1741.

[32] J. Jiang, J. A. Fan, Simulator-based training of generative neural networks for the inverse design of metasurfaces, Nanophotonics 9 (5) (2020) 1059–1069.

[33] Y. Augenstein, C. Rockstuhl, Inverse design of nanophotonic devices with structural integrity, ACS photonics 7 (8) (2020) 2190–2196.

[34] M. Barry, V. Berthier, B. Wilts, M.-C. Cambourieux, P. Bennet, R. Pollès, O. Teytaud, E. Centeno, N. Biais, A. Moreau, Evolutionary algorithms converge towards evolved biological photonic structures, Sci. Rep. 10 (2020) 12024. `doi:10.1038/s41598-020-68719-3`.

[35] Z. Lin, C. Roques-Carmes, R. Pestourie, M. Soljačić, A. Majumdar, S. G. Johnson, End-to-end nanophotonic inverse design for imaging and polarimetry, Nanophotonics 10 (3) (2021) 1177–1187.

[36] M. Zhou, D. Liu, S. W. Belling, H. Cheng, M. A. Kats, S. Fan, M. L. Povinelli, Z. Yu, Inverse design of metasurfaces based on coupled-mode theory and adjoint optimization, ACS Photonics 8 (8) (2021) 2265–2273.

[37] Y. Deng, S. Ren, K. Fan, J. M. Malof, W. J. Padilla, Neural-adjoint method for the inverse design of all-dielectric metasurfaces, Optics Express 29 (5) (2021) 7526–7534.

[38] P. Bennet, P. Juillet, S. Ibrahim, V. Berthier, M. A. Barry, F. Réveret, A. Bousquet, O. Teytaud, E. Centeno, A. Moreau, Analysis and fabrication of antireflective coating for photovoltaics based on a photonic-crystal concept and generated by evolutionary optimization, Phys. Rev. B 103 (12) (2021) 125135.

[39] F. Getman, M. Makarenko, A. Burguete-Lopez, A. Fratalocchi, Broadband vectorial ultrathin optics with experimental efficiency up to 99% in the visible region via universal approximators, Light: Science & Applications 10 (1) (2021) 1–14.

[40] E. Bayati, R. Pestourie, S. Colburn, Z. Lin, S. G. Johnson, A. Majumdar, Inverse designed extended depth of focus meta-optics for broadband imaging in the visible, Nanophotonics 11 (11) (2022) 2531–2540.

[41] E. Hassan, A. C. Lesina, Topology optimization of dispersive plasmonic nanostructures in the time-domain, Optics Express 30 (11) (2022) 19557–19572.

[42] Q. Wang, M. Makarenko, A. B. Lopez, F. Getman, A. Fratalocchi, Advancing statistical learning and artificial intelligence in nanophotonics inverse design, Nanophotonics 11 (11) (2022) 2483–2505.

[43] L. Novotny, B. Hecht, Principles of nano-optics, Cambridge university press, 2012.

[44] H. K. Baghbadorani, D. Aurelio, J. Barvestani, M. Liscidini, Guided modes in photonic crystal slabs supporting bloch surface waves, JOSA B 35 (4) (2018) 805–810.

[45] Y. Augenstein, A. Vetter, B. V. Lahijani, H. P. Herzig, C. Rockstuhl, M.-S. Kim, Inverse photonic design of functional elements that focus bloch surface waves, Light: Science & Applications 7 (1) (2018) 1–9.

[46] U. Stella, L. Boarino, N. De Leo, P. Munzert, E. Descrovi, Enhanced Directional Light Emission Assisted by Resonant Bloch Surface Waves in Circular Cavities, ACS Photonics 6 (8) (2019) 2073–2082. `doi:10.1021/acsphotonics.9b00570`.

[47] F. Wang, B. S. Lazarov, O. Sigmund, On projection methods, convergence and robust formulations in topology optimization, Struct. Multidisc. Optim. 43 (6) (2011) 767–784. `doi:10.1007/s00158-010-0602-y`.

[48] M. Zhou, B. S. Lazarov, F. Wang, O. Sigmund, Minimum length scale in topology optimization by geometric constraints, Compu. Methods Appl. Mech. Eng. 293 (2015) 266–282. `doi:10.1016/j.cma.2015.05.003`.

[49] B. S. Lazarov, F. Wang, O. Sigmund, Length scale and manufacturability in density-based topology optimization, Arch. Appl. Mech. 86 (1) (2016) 189–218. `doi:10.1007/s00419-015-1106-4`.

[50] K. Svanberg, A Class of Globally Convergent Optimization Methods Based on Conservative Convex Separable Approximations, SIAM J. Optim. 12 (2) (2002) 555–573. `doi:10.1137/S1052623499362822`.

[51] S. G. Johnson, stevengj/nlopt (Apr. 2020).

[52] O. Sigmund, Morphology-based black and white filters for topology optimization, Struct. Multidisc. Optim. 33 (4) (2007) 401–424. `doi:10.1007/s00158-006-0087-x`.

[53] A. F. Oskooi, D. Roundy, M. Ibanescu, P. Bermel, J. D. Joannopoulos, S. G. Johnson, Meep: A flexible free-software package for electromagnetic simulations by the FDTD method, Comput. Phys. Commun. 181 (3) (2010) 687–702. `doi:10.1016/j.cpc.2009.11.008`.

[54] A. M. Hammond, A. F. Oskooi, M. Chen, Z. Lin, S. G. Johnson, S. E. Ralph, High-performance hybrid time/frequency-domain topology optimization for large-scale photonics inverse design, Opt. Express 30 (3) (2022) 4467–4491. `doi:10.1364/OE.442074`.

[55] HIPS/autograd, Harvard Intelligent Probabilistic Systems Group (Apr. 2020).

[56] S. G. Johnson, J. D. Joannopoulos, Block-iterative frequency-domain methods for maxwell's equations in a planewave basis, Optics express 8 (3) (2001) 173–190.

[57] Z. Jin, S. Mei, S. Chen, Y. Li, C. Zhang, Y. He, X. Yu, C. Yu, J. K. Yang, B. Luk'yanchuk, et al., Complex inverse design of meta-optics by segmented hierarchical evolutionary algorithm, ACS nano 13 (1) (2019) 821–829.

[58] M. Makarenko, Q. Wang, A. Burguete-Lopez, F. Getman, A. Fratalocchi, Robust and scalable flat-optics on flexible substrates via evolutionary neural networks, Advanced Intelligent Systems 3 (11) (2021) 2100105.

[59] J. Lim, D. Psaltis, Maxwellnet: Physics-driven deep neural network training based on maxwell's equations, Apl Photonics 7 (1) (2022) 011301.

[60] M. Chen, R. Lupoiu, C. Mao, D.-H. Huang, J. Jiang, P. Lalanne, J. A. Fan, High speed simulation and freeform optimization of nanophotonic devices with physics-augmented deep learning, ACS Photonics (2022).